REPORT

APPLIED OPTICS

Imaging-based molecular barcoding with pixelated dielectric metasurfaces

Andreas Tittl[1], Aleksandrs Leitis[1], Mingkai Liu[2], Filiz Yesilkoy[1], Duk-Yong Choi[3], Dragomir N. Neshev[2], Yuri S. Kivshar[2], Hatice Altug[1]*

Metasurfaces provide opportunities for wavefront control, flat optics, and subwavelength light concentration. We developed an imaging-based nanophotonic method for detecting mid-infrared molecular fingerprints, and implemented it for the chemical identification and compositional analysis of surface-bound analytes. Our technique features a two-dimensional pixelated dielectric metasurface with a range of ultrasharp resonances, each tuned to a discrete frequency; this enables molecular absorption signatures to be read out at multiple spectral points, and the resulting information is then translated into a barcode-like spatial absorption map for imaging. The signatures of biological, polymer, and pesticide molecules can be detected with high sensitivity, covering applications such as biosensing and environmental monitoring. Our chemically specific technique can resolve absorption fingerprints without the need for spectrometry, frequency scanning, or moving mechanical parts, thereby paving the way toward sensitive and versatile miniaturized mid-infrared spectroscopy devices.

The mid-infrared (mid-IR) spectrum is essential for sensing because of the presence of characteristic molecular absorption fingerprints originating from the intrinsic vibrational modes of chemical bonds. Mid-IR spectroscopy allows direct characterization of molecular structures with chemical specificity unique to this spectral range, and is therefore widely recognized as the gold standard for chemical analysis (*1*). It is also a powerful non-destructive and label-free technique for identifying biochemical building blocks, including proteins, lipids, and DNA. However, because of the mismatch between mid-IR wavelengths and dimensions of molecules, the sensitivity of mid-IR spectroscopy is limited when detecting signals from nanometer-scale samples (*2*), biological membranes (*3*), or low numbers of surface-bound molecules (*4*).

Nanophotonics can overcome this limitation by exploiting the strong near-field enhancement of subwavelength resonators. When the resonance is spectrally overlapped with the absorption fingerprints, the enhanced molecule-resonator coupling can lead to a change in either the frequency or the strength of the resonance, from which the molecular fingerprints can be extracted. This concept, surface-enhanced infrared absorption (SEIRA), has been realized using various plasmonic platforms (*5*–*7*); however, the achieved performance is still far from ideal because of the inherent limitation of low-Q (quality factor) resonances imposed by resistive loss. Nanostructured resonators based on high-index dielectric materials offer low intrinsic loss and complementary metal-oxide semiconductor (CMOS) compatibility and have recently emerged as building blocks for various metadevices, with capabilities for controlling the propagation and localization of light (*8*, *9*). Many applications including generalized wavefront control (*10*, *11*), ultrathin optical elements (*12*, *13*), and antenna-based light concentration (*14*) have been shown experimentally. A key concept underlying the functionalities of many metasurface approaches is their use of constituent elements with spatially varying optical properties. The full potential of metasurface-based SEIRA with both spectral and spatial control over nanoscale field enhancement has yet to be realized.

We report a mid-IR nanophotonic sensor based on all-dielectric high-Q metasurface elements and demonstrate its capability for enhancing, detecting, and differentiating the absorption fingerprints of various molecules. Traditionally, high-Q resonances in metasurfaces are generated via the interference of superradiant and subradiant modes (*15*–*17*). In contrast, our design exploits the collective behavior of Mie resonances, which can be recognized as supercavity modes driven by the physics of bound states in the continuum (*18*). Furthermore, the high-Q resonances of our design are spectrally clean without additional resonance background, which is particularly attractive because it allows for the highly spectrally selective enhancement of spectroscopically rich molecular fingerprint information. Specifically, we implement a two-dimensional (2D) array of high-Q metasurface pixels, where the resonance positions of individual metapixels are linearly varied over a target mid-IR fingerprint range. This configuration allows us to assign each resonance position to a specific pixel of the metasurface, establishing a one-to-one mapping between spectral and spatial information (Fig. 1A). F1 By comparing the imaging-based readout of this spatially encoded vibrational information before and after the coating of target analyte molecules, we demonstrate chemically specific molecular barcodes suitable for chemical identification and compositional analysis.

Individual metapixels contain a zigzag array of anisotropic hydrogenated amorphous silicon (a-Si:H) resonators, which provide high-Q resonances when excited with linearly polarized light and allow for straightforward resonance tuning via scaling of its geometrical parameters by a factor S (Fig. 1B). Numerically simulated reflectance spectra of an exemplary 5 × 5 metasurface pixel array with a scaling factor variation from S = 1.0 to S = 1.3 show sharp resonance peaks (average Q > 200) with near-unity reflectance intensity and linear tunability of the resonance positions covering the spectral range from 1350 to 1750 cm^{-1} (Fig. 1C). Our metapixel design also provides enhancement of the local electric near-field intensity confined to the resonator surface by more than three orders of magnitude (*19*), which is ideal for the sensitive detection of analyte molecular vibrations (Fig. 1D and fig. S1). The target spectral range from 1350 to 1750 cm^{-1} contains characteristic molecular stretching and bending vibrations found in hydrocarbons and amino acids, making it crucial for detecting and differentiating the absorption signatures of biomolecules, environmental pollutants, and polymeric species, among others. We first focus on a biosensing application by showing chemical-specific protein detection, where the distinct protein absorption fingerprint is governed by the amide I and II vibrational bands located near 1660 cm^{-1} and 1550 cm^{-1}, respectively.

A sub–5-nm conformal protein layer covering the pixelated metasurface causes a pronounced modulation of the individual metapixel reflectance spectra due to the coupling between the molecular vibrations and the enhanced electric near-fields around the dielectric resonators. This reflectance modulation manifests primarily as an attenuation and broadening of the metapixel resonance, which are correlated with the strength of the amide I and II molecular vibrations (Fig. 1E). The envelope of the metapixel reflectance spectra unambiguously reproduces the protein absorption signature, confirming efficient molecular fingerprint detection. The metapixel resonances provide linewidths much narrower than the spectral feature size of the individual amide I and II absorption bands near 60 cm^{-1}. This is in strong contrast to metal-based antennas used in plasmonic SEIRA approaches, which typically exhibit linewidths above 200 cm^{-1} limited by the intrinsic damping of the metal (*5*). This advantage allows us to read out the protein absorption signature at multiple discrete frequency

[1]Institute of BioEngineering, École Polytechnique Fédérale de Lausanne (EPFL), Lausanne 1015, Switzerland. [2]Nonlinear Physics Centre, Research School of Physics and Engineering, Australian National University, Canberra, ACT 2601, Australia. [3]Laser Physics Centre, Research School of Physics and Engineering, Australian National University, Canberra, ACT 2601, Australia.
*Corresponding author. Email: hatice.altug@epfl.ch

points and to translate this spectrally resolved absorption information into a barcode-like spatial map of the individual metapixel absorption signals (Fig. 1F).

A pixelated dielectric metasurface design consisting of an array of 10 × 10 metapixels was fabricated using electron-beam lithography and reactive ion beam etching. Ellipse axes and unit cell periodicities were identical to the values given for the numerical simulations in Fig. 1, and the unit cell was linearly scaled between S = 1.00 and S = 1.34 in 100 steps. A fixed metapixel size of 100 μm × 100 μm was chosen to provide a trade-off between metapixel signal-to-noise ratio and number of pixels (Fig. 2A and fig. S2). Analysis of scanning electron microscopy (SEM) images captured for multiple metapixels confirmed the accurate reproduction of the resonator design as well as the linear scaling of the unit cell geometry over the entire metasurface area (Fig. 2B and fig. S3).

The metasurface was characterized in reflection using a quantum cascade laser-based mid-IR microscope equipped with a 480 × 480 pixel array-based imaging detector. We used a refractive 4× objective with a 2-mm field of view to acquire the optical response of all metasurface pixels simultaneously (Fig. 2C). Reflectance images captured for different wavenumbers of the incident mid-IR radiation are shown in Fig. 2D. At each incident wavenumber, high reflectance intensity indicates the excitation of a metapixel with matching resonance frequency in a specific spatial location on the metasurface. Reflectance spectra are obtained by combining reflectance images for a range of incident wavenumbers and integrating the resulting spectrally resolved data over the individual metapixel areas (*19*). The spectra of 21 exemplary metapixels and extracted resonance positions of all 100 metasurface pixels are shown in Fig. 2, E and F. The fabricated pixelated metasurface delivers resonances with low average full width at half maximum (FWHM) of 13.7 cm^{-1} and uniform tuning of the resonance frequency over the amide band range from 1370 to 1770 cm^{-1}. This corresponds to a spectral resolution of 4 cm^{-1} and an average Q of 115 (fig. S4), which is an improvement of more than one order of magnitude over metallic antenna geometries (*20*, *21*). Note that our design can easily be extended to cover a larger spectral region by increasing the range of geometrical scaling parameters (fig. S5).

We demonstrated molecular fingerprint detection by interrogating a physisorbed monolayer of recombinant protein A/G. Metapixel reflectance spectra before and after the protein A/G physisorption are shown in Fig. 3, A and B, respectively. All spectra are normalized to the peak reflectance values of the reference measurement without analyte. The absorbance signal calculated from the peak reflectance envelopes before (R_0) and after physisorption (R_S) reveals the characteristic amide I and II absorption signature of the

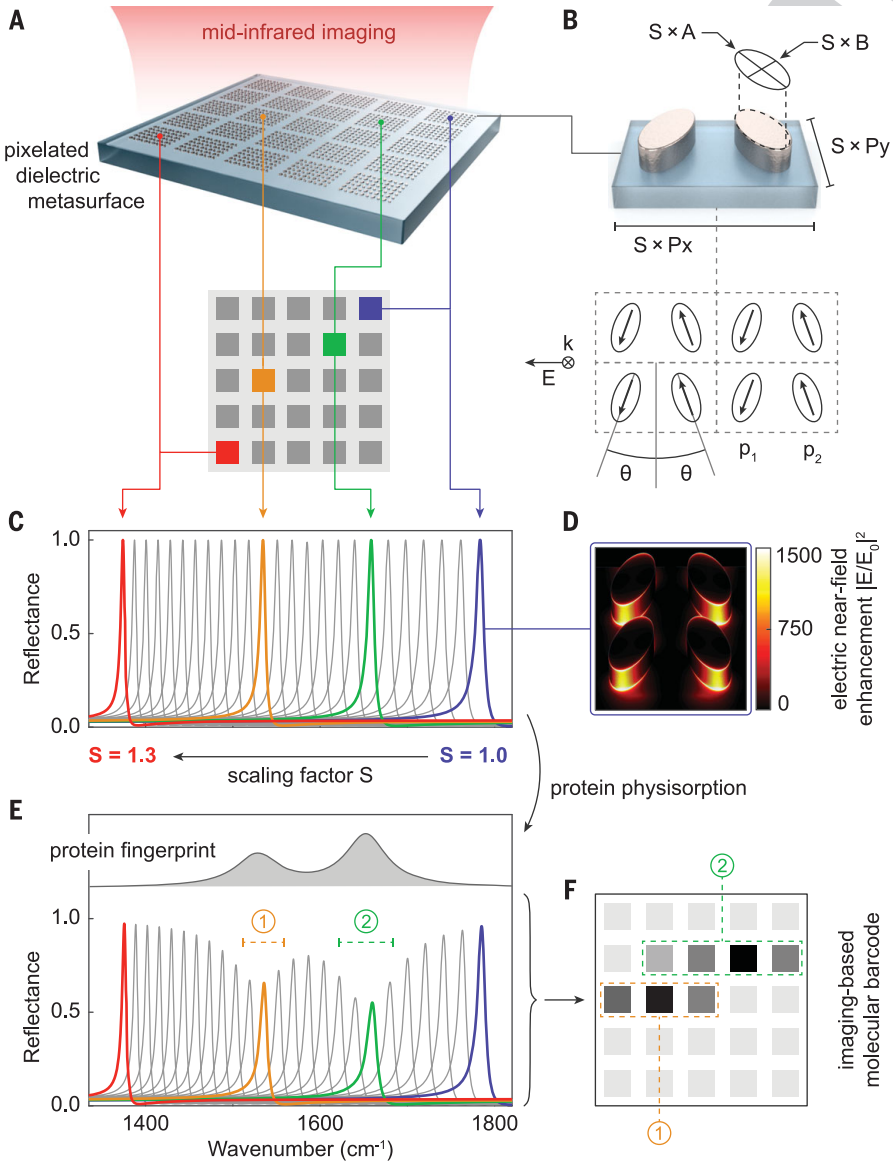

Fig. 1. Molecular fingerprint detection with pixelated dielectric metasurfaces. (**A**) Pixelated metasurface composed of a two-dimensional array of high-Q resonant metapixels with resonance frequencies tuned over a target molecular fingerprint range. (**B**) Spectrally clean high-Q (Q > 200) resonances are provided by zigzag arrays of anisotropic a-Si:H resonators. Resonance frequencies are controlled by scaling the unit cell lateral dimensions by a factor S. Geometrical parameters are A = 1.96 μm, B = 0.96 μm, Px = 3.92 μm, and Py = 2.26 μm, with a fixed structure height of H = 0.7 μm and an orientation angle of θ = 20°. (**C**) Numerically simulated metapixel reflectance spectra for different values of the scaling parameter S, chosen to cover the amide band spectral region around 1600 cm^{-1}. (**D**) Simulated electric near-field intensity enhancement $|E/E_0|^2$ for S = 1, where $|E_0|$ denotes the incident field amplitude. (**E**) The envelope of metapixel reflectance amplitudes reproduces the absorption fingerprint of an adjacent model protein layer (top inset). (**F**) Conceptual sketch of a molecule-specific barcode produced by imaging-based readout of the metasurface's reflectance response. Image regions 1 and 2 indicate the spatially encoded vibrational information from the corresponding metapixel resonances in (E).

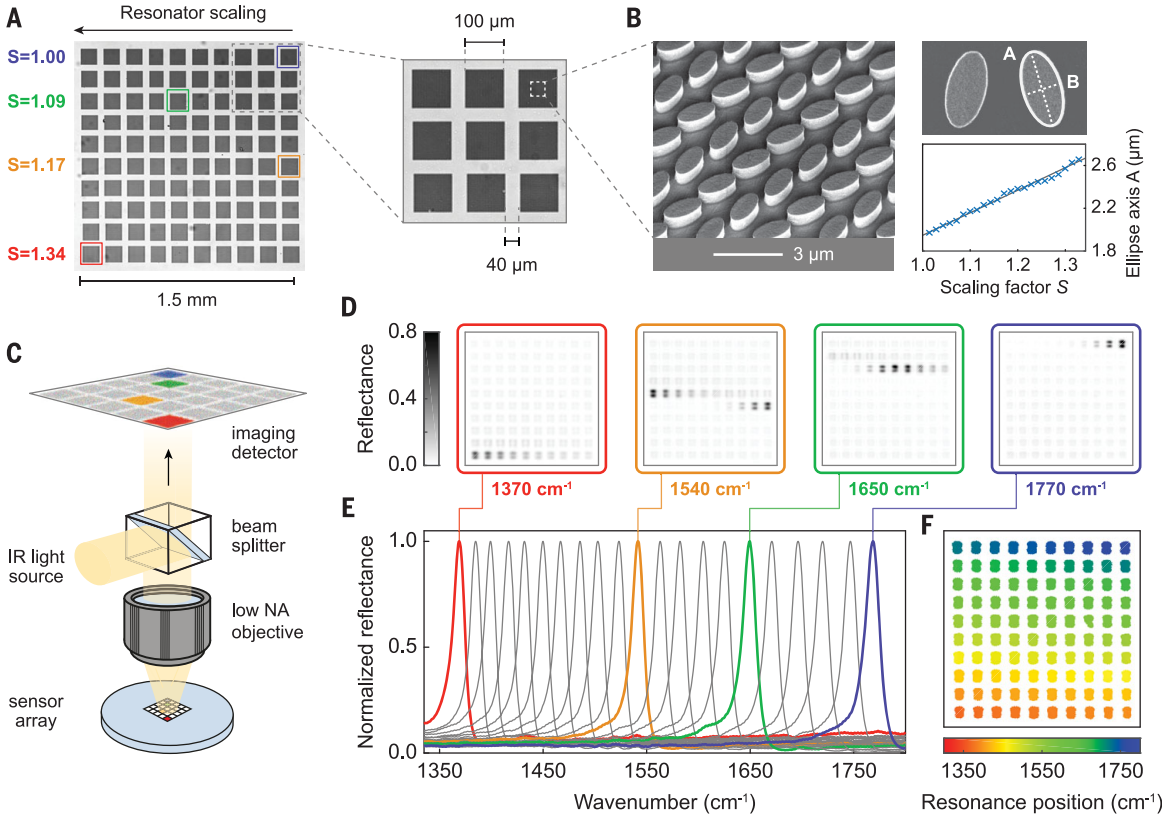

Fig. 2. Experimental realization of the pixelated metasurfaces. (**A**) Optical images of the fabricated 100-pixel metasurface. (**B**) SEM micrographs confirm the linear relationship between scaling factor and ellipse feature size. (**C**) Sketch of the imaging-based mid-IR microscopy system. (**D**) Reflectance images of the pixelated metasurface recorded at four specific wavenumbers in the mid-IR spectral range. (**E**) Normalized reflectance spectra for 21 of the 100 metapixels. Resonance positions of the colored curves correspond to the respective reflectance images in (D). (**F**) Extracted resonance positions for all metapixels.

protein A/G molecules, which is in good agreement with an independent infrared reflection-absorption spectroscopy (IRRAS) measurement (Fig. 3C). Furthermore, the high absorbance signal of up to A = 140 mOD extracted from a protein monolayer demonstrates the strong vibrational enhancement of our metasurface design, which exceeds the performance of widely used metal antenna geometries (*22*) by more than one order of magnitude (fig. S6). Combined with an experimental noise level of 1.8 mOD, this value corresponds to a detection limit of 2130 molecules/µm^2 (fig. S7).

Miniaturization of IR sensor devices has traditionally been challenging because of the need for scaled-down Fourier-transform (FTIR) spectrometers or frequency scanning laser sources (*23*). Recent sensor-on-chip approaches based on thin-film optical waveguides have made progress with monolithic integration, in which the light source, sensing element, and detector are fabricated on a single chip (*24*–*26*). In comparison, our technique enables a complementary integration scheme in which the pixelated metasurface sensor can be combined with an IR imaging detector such as a high-resolution microbolometer or a mercury cadmium telluride (MCT) focal plane array (fig. S8). When illuminated with an external broadband light source, this arrangement can overcome the need for a mid-IR spectrometer in a compact footprint. Furthermore, our scheme addresses several constraints of complete monolithic integration, such as the limited operating range of chip-based light sources and detectors (*27*), as well as sensitivity limitations caused by the low near-field enhancement factors of conventional waveguides (*26*).

We assessed the capability of our metasurface sensor for imaging-based spectrometerless fingerprint detection by calculating the integrated reflectance signal from the spectral data of each metapixel. These integrated signals are analogous to a readout of the metasurface's optical response with a broadband detector before (I_0) and after (I_S) addition of the protein layer (Fig. 3D) and are used to calculate metapixel absorbance signals via $A = -\log(I_S/I_0)$, which are then rescaled from 0 to 100 (Fig. 3E). The resulting barcode-like spatial absorption map of the protein A/G monolayer clearly shows the spectral location and relative intensity distribution of the characteristic amide I and II absorption bands as two distinct high-signal regions of the image, providing chemically specific fingerprint detection in a miniaturized design and without the need for spectrometry. This functionality is enabled by the spectrally clean high-Q resonances of the dielectric metapixels and cannot be achieved with metapixels based on conventional metal antennas as a result of linewidth limitations (fig. S9). In addition to protein A/G, we also tested a polymer mixture composed of polymethyl methacrylate (PMMA) and polyethylene (PE) as well as glyphosate pesticide to cover applications in fields as diverse as biosensing, materials science, and environmental monitoring. In all three cases, the molecular barcodes feature mutually distinct high-intensity image regions unique to the vibrational signature of the investigated analytes (Fig. 4A), underscoring the chemical identification capability. F4

Our barcoding technique offers the potential for identifying molecular species in arbitrary analyte compositions through pattern recognition based on a library of multiple molecular barcode signatures (fig. S10). To illustrate this approach, we detected a series of predefined mixtures of PMMA and PE polymer molecules deposited on the metasurface by thermal evaporation. Figure 4B shows molecular barcodes for pure PMMA and PE as well as PMMA/PE mixing ratios of 0.25, 0.50, and 0.75. The characteristic molecular signatures of PMMA and PE appear as distinct image features in the top and bottom halves of the barcode matrix, respectively. When increasing the relative amount of PE in the mixture, we observed a substantial increase of the

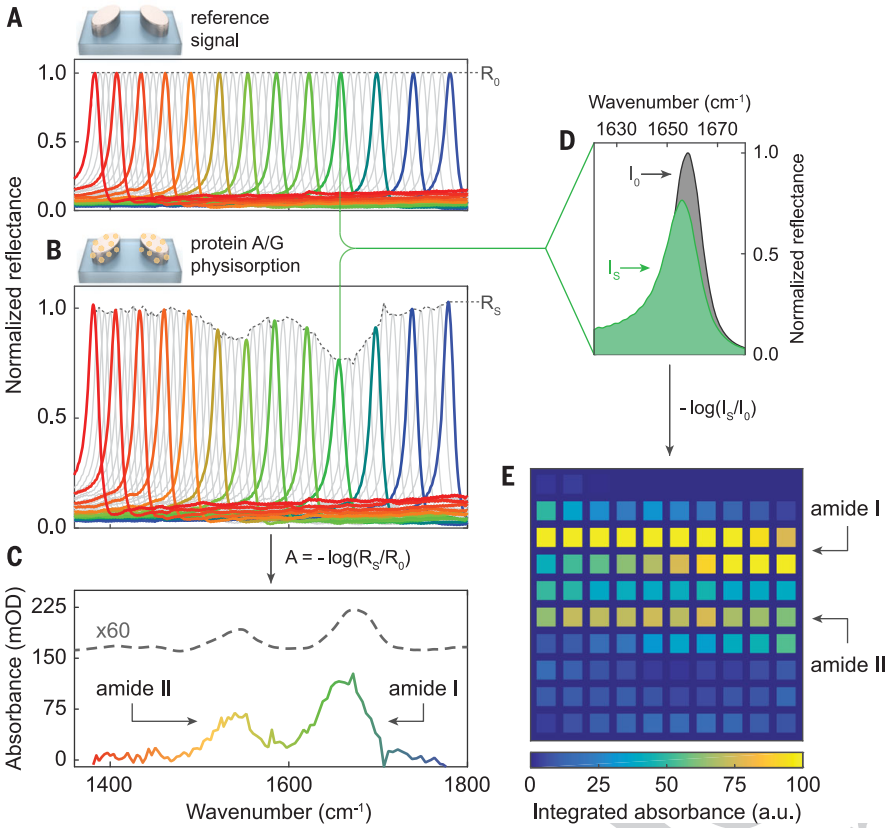

Fig. 3. Molecular fingerprint retrieval and spatial absorption mapping. (**A**) Normalized metapixel reflectance spectra before physisorption of a protein A/G monolayer. R_0 indicates the envelope of peak reflectance amplitudes (dashed line). (**B**) Normalized spectra after protein physisorption, including reflectance envelope R_S (dashed line). (**C**) Protein absorption fingerprint calculated from the reflectance envelopes R_0 and R_S compared to an independent IRRAS measurement (dashed line, scaled and offset for clarity). (**D**) Broadband spectrometerless operation of the metasurface can be emulated by integrating the reflectance signal of all pixels. (**E**) Spectral integration translates the absorption signature in (C) into a 2D spatial absorption map, which represents the molecular barcode of the protein (a.u., arbitrary units).

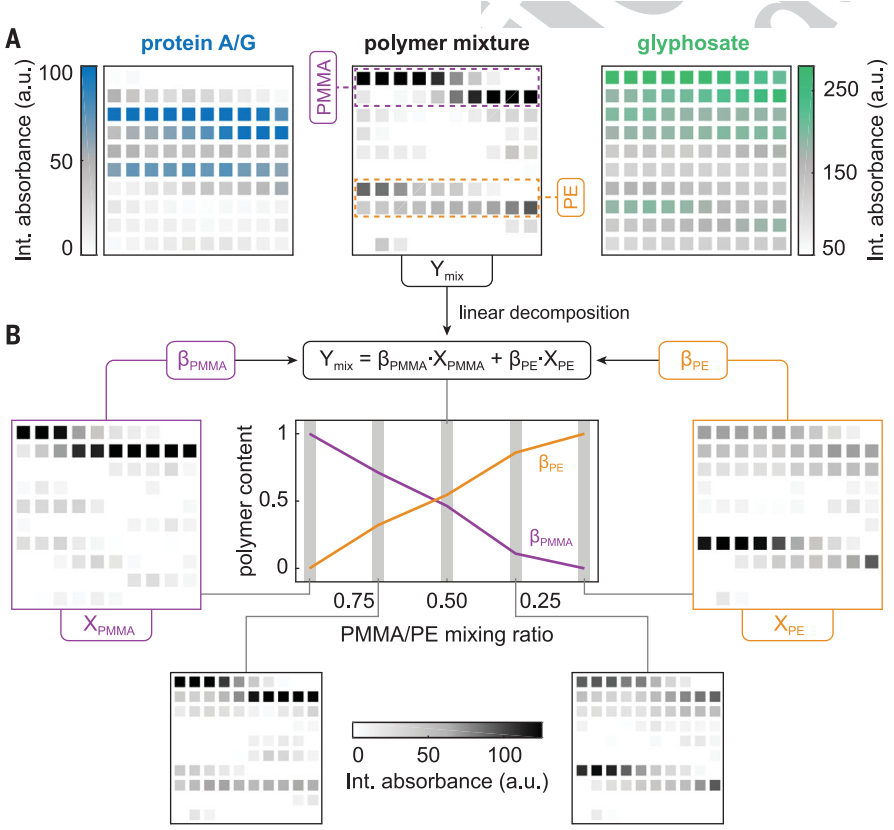

Fig. 4. Imaging-based chemical identification and compositional analysis. (**A**) Molecular barcodes of protein A/G, a mixture of PMMA and PE polymers, and glyphosate pesticide reveal the distinct absorption fingerprints of the analytes. (**B**) Barcode matrices for PMMA/PE polymer mixtures with several mixing ratios. Linear decomposition analysis of all mixing states Y_{mix} with respect to the pure PMMA and PE barcode matrices confirms accurate readout of the deposited polymer ratios.

PE signal versus mixing ratio combined with an associated decrease of the PMMA signal.

We carried out further image-based analysis by decomposing the barcode matrices of all mixing states Y_{mix} into a linear combination of the PMMA and PE molecular barcodes according to

$$Y_{mix} = (\beta_{PMMA} \cdot X_{PMMA}) + (\beta_{PE} \cdot X_{PE}) \quad (1)$$

where X_{PMMA} and X_{PE} are the input barcodes of the pure materials, and β_{PMMA} and β_{PE} are the output coefficients associated with the analyte content on the surface (Fig. 4B, center). The PMMA and PE polymer amounts obtained from our image decomposition analysis accurately captured the linear variation of the polymer composition, highlighting the rich chemical and compositional information available from such absorption maps. Although simple linear decomposition is implemented in this demonstration, nonlinear processes (such as those in biomolecular interactions involving multiple analytes and kinetics) are foreseen to make use of more sophisticated neural network–based image recognition methods and machine learning (*28*, *29*).

Our nanophotonic technique offers the prospect of IR absorption spectroscopy without the need for complex instrumentation. The Si-based pixelated metasurface is compatible with CMOS technology for low-cost wafer-scale sensor fabrication and can be combined with state-of-the-art surface functionalization techniques for operation in more complex bioassays (*30*). The sensitivity and *Q*-factor of our metasurface can be further improved by decreasing the resonator orientation angle, limited only by the inhomogeneity of the nanofabrication. Additionally, even stronger near-field enhancement could be achieved by using more sophisticated designs for meta-atoms. The molecular barcodes obtained with our method offer unique possibilities for advanced image analysis, paving the way toward versatile and sensitive miniaturized mid-IR spectroscopy devices.

REFERENCES AND NOTES

1. B. H. Stuart, *Infrared Spectroscopy: Fundamentals and Applications* (Wiley, 2005).
2. D. Dregely, F. Neubrech, H. Duan, R. Vogelgesang, H. Giessen, *Nat. Commun.* **4**, 2237 (2013).
3. O. Limaj *et al*., *Nano Lett.* **16**, 1502–1508 (2016).
4. C. Huck *et al*., *ACS Nano* **8**, 4908–4914 (2014).
5. F. Neubrech, C. Huck, K. Weber, A. Pucci, H. Giessen, *Chem. Rev.* **117**, 5110–5145 (2017).
6. L. Dong *et al*., *Nano Lett.* **17**, 5768–5774 (2017).
7. B. Cerjan, X. Yang, P. Nordlander, N. J. Halas, *ACS Photonics* **3**, 354–360 (2016).
8. A. I. Kuznetsov, A. E. Miroshnichenko, M. L. Brongersma, Y. S. Kivshar, B. Luk'yanchuk, *Science* **354**, aag2472 (2016).
9. A. Y. Zhu, A. I. Kuznetsov, B. Luk'yanchuk, N. Engheta, P. Genevet, *Nanophotonics* **6**, 1–20 (2017).
10. A. Arbabi, Y. Horie, M. Bagheri, A. Faraon, *Nat. Nanotechnol.* **10**, 937–943 (2015).
11. M. Decker *et al*., *Adv. Opt. Mater.* **3**, 813–820 (2015).
12. M. Khorasaninejad *et al*., *Science* **352**, 1190–1194 (2016).
13. D. Lin, P. Fan, E. Hasman, M. L. Brongersma, *Science* **345**, 298–302 (2014).
14. M. Caldarola *et al*., *Nat. Commun.* **6**, 7915 (2015).
15. M. F. Limonov, M. V. Rybin, A. N. Poddubny, Y. S. Kivshar, *Nat. Photonics* **11**, 543–554 (2017).
16. C. Wu *et al*., *Nat. Commun.* **5**, 3892 (2014).
17. S. Campione *et al*., *ACS Photonics* **3**, 2362–2367 (2016).
18. M. Rybin, Y. Kivshar, *Nature* **541**, 164–165 (2017).
19. See supplementary materials.
20. K. Chen, R. Adato, H. Altug, *ACS Nano* **6**, 7998–8006 (2012).
21. C. Wu *et al*., *Nat. Mater.* **11**, 69–75 (2011).
22. S. Bagheri *et al*., *ACS Photonics* **2**, 779–786 (2015).
23. F. K. Tittel, D. Richter, A. Fried, in *Solid-State Mid-Infrared Laser Sources*, I. T. Sorokina, K. L. Vodopyanov, Eds. (Springer, 2003), pp. 458–529.
24. B. Schwarz *et al*., *Nat. Commun.* **5**, 4085 (2014).
25. A. Harrer *et al*., *Sci. Rep.* **6**, 21795 (2016).
26. M. Sieger, B. Mizaikoff, *Anal. Chem.* **88**, 5562–5573 (2016).
27. H. Lin *et al*., *Nanophotonics* **7**, 393–420 (2017).
28. G. E. Hinton, R. R. Salakhutdinov, *Science* **313**, 504–507 (2006).
29. Y. LeCun, Y. Bengio, G. Hinton, *Nature* **521**, 436–444 (2015).
30. S. Jiang *et al*., *Nanoscale* **5**, 3127–3148 (2013).

ACKNOWLEDGMENTS

We thank R. Guo, E. Romero Arvelo, and D. Rodrigo for useful discussions, and École Polytechnique Fédérale de Lausanne and Center of MicroNano Technology for nanofabrication. Sample fabrication was performed in part at the ACT node of the Australian National Fabrication Facility. **Funding:** The research leading to these results has received funding from the European Research Council under grant agreement no. 682167 VIBRANT-BIO and the European Union Horizon 2020 Framework Programme for Research and Innovation under grant agreements no. 665667 (call 2015), no. 777714 (NOCTURNO project), and no. 644956 (RAIS project). The authors acknowledge the support of the Australian Research Council. **Author contributions:** A.T., D.N.N., Y.S.K., and H.A. conceived and designed the research; A.L., F.Y., and D.-Y.C. fabricated the dielectric metasurfaces; A.T. and A.L. carried out optical measurements and analyzed data; A.L. and M.L. carried out numerical simulations; and all authors contributed to writing the manuscript. **Competing interests:** None declared. **Data and materials availability:** All data needed to evaluate the conclusions in the paper are present in the paper or the supplementary materials.

SUPPLEMENTARY MATERIALS

www.sciencemag.org/content/360/63XX/PAGE/suppl/DC1
Materials and Methods
Supplementary Text
Figs. S1 to S10
References (*31*–*34*)

24 January 2018; accepted 13 April 2018
10.1126/science.aas9768